Full Length Article

Size-miniaturization of TiO$_2$-ZrO$_2$ coupled semiconductors to develop highly efficient visible- driven photocatalysts for the degradation of drugs in wastewater

Jhon Mauricio Aguirre-Cortés, Álvaro Munguía-Ubierna, Adriana Moral-Rodríguez, A.F. Pérez-Cadenas, F. Carrasco-Marín, E. Bailón-García *

UGR-Carbon: Carbon-based Polyfunctional Materials, Department of Inorganic Chemistry, Faculty of Sciences, University of Granada, Campus Fuente Nueva s/n, 18071, Granada, Spain

ARTICLE INFO

ABSTRACT

Solar photocatalysis has emerged as a cost-effective and efficient approach to address water remediation challenges. Nonetheless, there is a pressing requirement to innovate and design novel photocatalysts capable of utilizing solar or visible light. In this study, morphology control and surface sensitization techniques were integrated to engineer titania-based photocatalysts that operate efficiently under blue LED light. This is accomplished through the synthesis of Ti$_a$Zr$_b$O$_c$ materials (TiXZrY) with finely tuned nano-scale dimensions, employing meticulous control through the reversed two-emulsion technique. This innovative approach has yielded remarkable performance in the removal of pharmaceutical contaminants. Zr contents highly affect the size and, thus, the active surface of the photocatalysts. XRD results indicate that a low Zr content zirconium titanates are formed whereas at high Zr contents zirconia cubic phase is the main crystalline structure detected. The heterojunction created between the zirconium titanate and the titania anatase phases can be responsible of the band gap reduction observed (Eg = 2.8 eV). A SMX degradation percent as high as 80.1 % with a decrease of the treated water toxicity was obtained for Ti70Zr30 under blue-LEDs irradiation which is explained based on the formation of zirconium titanates observed by XRD and XPS and the high active surface area.

1. Introduction

Emerging pollutants (EPs) are increasingly detected in wastewater, which is causing global concern. Among these emerging pollutants, the most worrying ones due to the high consumption in recent years are pharmaceuticals, antibiotics, and drugs of abuse. Global consumption of pharmaceuticals is estimated at thousands of tons per year. These EPs exhibit remarkable persistence and have the tendency to accumulate in the environment, thereby posing a significant threat to both human health and ecosystems. Some researchers have addressed the EPs ecotoxicity on plants and fauna. Sublethal effects (oxidative stress) have been observed on zebra mussel after 14 days of exposition to 0.5 and 1 μg L^{-1} solutions of the cocaine metabolite benzoylecgonine (a similar concentration to those found in wastewater). The mussels also displayed oxidative alterations in various categories of proteins [1]. Estrogens and estrogen mimics have an impact on the reproductive well-being of wild fish species. Kidd *et al.* [2] found that a continuous exposure of fathead

minnow to a low concentration (5–6 ng L^{-1}) of synthetic estrogen, 17α-ethynylestradiol, resulted in several notable effects, including the feminization of males, noticeable impacts on gonadal development, such as intersex occurrences in males, and alterations in oogenesis in females. Furthermore, it had such a significant impact that it nearly led to the extinction of this species within the lake. This underscores the potential threat posed by the presence of estrogens in freshwater environments, as it can significantly affect the sustainability of wild fish populations. Paracetamol is another priority pharmaceutical with potential toxicity to freshwater organisms. Osazee *et al.* [3] investigated the impact of paracetamol on African catfish embryos and larvae. Their study revealed that the exposition of embryos to paracetamol led to several concerning outcomes, including a reduction in hatching rates, the onset of erratic swimming behavior in catfish, a significant decrease in heartbeat rate, and the emergence of teratogenic, neurotoxic, and cardiotoxic effects. This study demonstrates that the presence of paracetamol in freshwater affects the survival of aquatic life, particularly catfish. In turn, the

presence of antibiotics in aquatic environments has been linked to the emergence of drug-resistant bacteria and drug-resistant gene transmission [4]. In particular, sulfonamide antibiotics can inhibit the growth of algae and cyanobacteria, which are crucial components of the aquatic food chain [5,6]. Yan *et al.* [7] demonstrated that the antibiotic sulfamethazine had toxic effects on both embryos and adult zebrafish, leading to morphological deformities such as edema and spinal curvature during the embryo-larval stages. Sulfamethoxazole (SMX) is particularly concerning because it exhibits the lowest removal efficiency in wastewater treatment plants [8]. Xu *et al.* [9] observed that exposure of algae to SMX resulted in altered gene expression, leading to changes in algal cell ultrastructure and inhibiting cell growth. Furthermore, SMX was found to influence non-coding RNA metabolic processes, ultimately affecting nuclear structures and promoting the occurrence, invasion, and metastasis of tumors.

Despite the demonstrated toxicity of these emerging pollutant to the water ecosystems, there is no regulation for most of these pollutants and they are not effectively removed by conventional wastewater treatment processes [10,11] making this uncontrolled discharge of drugs into water ecosystems, a serious problem that must be addressed. Thus, new removal methods for the treatment of wastewater must be designed to ensure the quality and bioprotection of water ecosystems.

The degradation of pollutants through photocatalysis is primarily achieved using conventional ultraviolet lamps, typically mercury vapor lamps. However, these lamps have drawbacks, such as high energy consumption, hazardous mercury content, the need for cooling, short lifespan, and operational complexities. Therefore, solar photocatalysis emerges as an effective and economical method for water remediation. This method relies solely on solar light and oxygen as reagents, and it operates under standard atmospheric pressure and temperature conditions. Nonetheless, there is a need to develop new photocatalysts that can harness solar or visible light effectively since titania, the most used photocatalyst, requires the use of UV irradiation for its activations due to its high band gap (3.2 eV). Moreover, titania suffers high rates of electron-hole recombination and a limited surface area, both of which contribute to a decrease in its photocatalytic efficiency. Thus, the strategies in existing literature to improve visible light response and photoactivity of TiO_2 follow two main routes: i) titania doping with heteroatoms (metal [12–14] or non-metal [12,15]) or surface sensitization by narrow band gap semiconductor [16–19], carbon materials [20–22], organic dyes [23,24], inorganic metal complexes [25–27] or conjugated polymers [28–30] to narrow the band-gap energy, enabling the utilization of the large fraction of solar spectrum and ii) morphology control of titania to increase the active surface area while minimizing the electron-hole recombination probability [31–34]. Despite the advances in the synthesis of solar-driven photocatalysis, using solar light for photocatalysis requires a vast area for effective application, leading to high installation costs and limitations to daylight hours, which significantly hinders the development and effective utilization of photocatalytic processes and reactors [35,36]. Light emitting diodes (LEDs) emitting electromagnetic radiation in the visible wavelengths have garnered increasing attention in recent years. LEDs are compact, durable, mercury-free, safe, energy efficient and boast a longer lifespan compared to conventional light sources [37,38]. Moreover, they can function on direct current. These attributes make LEDs a promising alternative to traditional ultraviolet sources, presenting new opportunities for photocatalytic degradation with lower power consumption and increased flexibility in designing various types of photocatalytic reactors.

In this study, we integrate both approaches to create titania-based photocatalysts driven by blue LED light, achieving exceptional performance in the degradation of pharmaceutical compounds found in wastewater. This is accomplished through the synthesis of $Ti_XZr_YO_Z$ materials with nano-scale dimensions and precise control over their crystalline phases. Comprehensive characterization and testing of these materials were conducted, focusing on their effectiveness in

sulfamethoxazole degradation under Blue-LEDs irradiation.

2. Experimental

2.1. Synthesis of TiO₂-ZrO₂ nanoparticles

TiO_2-ZrO_2 nanoparticles were obtained using the reversed two-emulsion method [39,40] with zirconium(IV) oxynitrate hydrate and titanium tetrachloride serving as precursors for ZrO_2 and TiO_2, respectively. Briefly, two emulsions were prepared using 228 g of n-heptane, 74 g of Triton X-100, and 58 g of hexanol. In the first microemulsion, the appropriate amounts of zirconium and titanium precursors were dissolved, while the second microemulsion substituted the metal precursors with tetramethylammonium hydroxide dissolved in 80 mL of water. Both microemulsions were mixed and vigorously stirred for 24 h. The resulting solid was recovered through centrifugation at 13000 rpm for 30 min, washed multiple times with ethanol, and finally dried at 80 °C before being calcined at 400 °C for 2 h (based on the results from the thermogravimetric analysis). The samples were labeled with the notation TiXZrY, where X and Y represent the weight percentages of TiO_2 and ZrO_2 in the sample, respectively. For instance, Ti10Zr90 signifies that the nanoparticles contain 10 wt% of TiO_2 and 90 % of ZrO_2.

2.2. Textural and chemical characterization

The textural characteristics of the samples were assessed using N_2 adsorption–desorption at −196 °C. To prepare the samples, they were first subjected to overnight outgassing at 110 °C under a high vacuum level of 10^{-6} mbar. Then, adsorption data were utilized to derive several important parameters. Specifically, the specific surface area (S_{BET}), and micropore volume (W_0), and mean width (L_0) were determined by applying the BET and Dubinin-Radushkevich (DR) equations, respectively. The total pore volume ($V_{0.95}$) was calculated based on the N_2 adsorption volume at a relative pressure of 0.95. Lastly, the mesopore volume (V_{MESO}) was computed using the Gurvich rule as $V_{0.95}$ minus $W_0(N_2)$.

The texture and morphology of samples were examined through high-resolution electron microscopy (HRTEM) utilizing a Thermo Fisher Scientific microscope model Talos F200X. For this, the samples were ground finely and dispersed with the aid of ultrasound, in an ethanol suspension and then depositing droplets of the suspension on a Cu grid, coated with a holey amorphous carbon film.

X-ray diffraction analysis was conducted to assess the crystallinity of samples. This analysis was carried out using a Bruker D8 Venture X-ray diffractometer equipped with Cu Kα radiation (λ = 0.155418 nm). XRD patterns were recorded over a 2θ range spanning from 5° to 75°. The Debye-Scherrer equation was employed on the predominant diffraction peak to determine the average crystal size of the metal.

Raman spectra were acquired using a JASCO NRS-5100 dispersive spectrophotometer with a 532 nm laser line. Each spectrum was obtained as an average of 64 scans obtained with 85 mW laser power.

X-ray photoelectron spectroscopy (XPS) was carried out using a Kratos Axis Ultra-DLD spectrometer, equipped with a hemispherical electron analyzer connected to a DLD (delay-line detector), a dual anode X-ray source (Mg/Al) with a power output of 450 W and an Al-Kα monochromator with a power rating of 600 W. The XPS spectra were acquired using monochromatic Al Kα radiation. The equipment is also provided with an electron source for charge neutralisation. The binding energy of photoelectron peaks was calibrated with respect to the C1s core level of adventitious carbon at 284.8 eV. High-resolution spectra were captured with a concentric hemispherical analyzer set at a take-off angle of 45°. The analyzer operated in constant pass energy mode at 29.35 eV, employing a 720 µm diameter aperture. Throughout spectrum acquisition, the residual pressure in the analysis chamber remained below 1.33×10^{-7} Pa. Samples were affixed to a holder using a carbon conductive tape and subjected to overnight vacuum in the preparation

chamber before transferring to the spectrometer's analysis chamber. Each spectral region underwent scanning in two separate areas, employing multiple sweeps until a satisfactory signal-to-noise ratio was achieved. The spectra obtained after background signal correction (Shirley-type background) were fitted to Lorentzian and Gaussian curves in order to obtain the number of components, the position of each peak, and the peak areas.

Thermogravimetric analysis (TGA) was conducted utilizing a METTLER-TOLEDO TGA/DSC1 Thermogravimetric Analyzer, while an Optima 8300 ICP-OES system from Perkin-Elmer was employed for elemental analysis.

The optical absorption spectra of the samples were acquired using a VARIAN CARY 5E double-beam UV–vis spectrophotometer, which was outfitted with a Praying Mantis diffuse reflectance accessory (DRS). The reflectance spectra were then analyzed using the Kulbelka–Munk (KM) method to determine the band gap (E_g) of the samples.

2.3. Photocatalytic tests

The photoactive properties of the synthesized photocatalysts were assessed in the photodegradation of an emerging drug; sulfamethoxazole (SMX) under blue led light irradiation using two 50 w LED chips (465 nm main emission, total electric power ~100 W and 4080 lm/W), **Figure S1**. For this, a borosilicate glass reactor was placed between both led chips (Fig. 1). The power density was 1.2 W/cm^2. The pH of the experiments at the beginning was adjusted to 7, with different solutions of NaCl and HCl (0.01 N), and during the kinetic, the temperature was maintained at 30 °C. Before exposure to light, the catalysts (100 mg) were immersed in a pollutant solution (100 mL) and allowed to reach adsorption–desorption equilibrium under stirring in the dark. The initial concentration of the pollutant in the solution was adjusted to achieve a final concentration of 5 mg/L, a value determined based on the SMX adsorption isotherms on the materials. To assure the adsorption–desorption equilibrium, the suspensions were stirred at 220 rpm for 12 h in the darkness before exposure to irradiation. Afterwards, 1.5 mL was sampled to extract only 10 % of the volume total. Then the aliquots were filtered and the SMX concentration was determined in a UV–Vis 6505 JENWAY Spectrophotometer by registering the SMX maximum absorption at the wavelength of 258 nm.

Toxicity assessments were carried out on solutions, both before and after catalytic degradation. These tests were conducted using the normalized biotest (UNE/EN/ISO 11345-2), which measures luminescent inhibition in *Vibrio fischeri* bacteria. The assessments were performed with the LUMIStox 300 system from Dr. LangeGmbH, coupled with a LUMIStherm incubator. Toxicity levels were quantified as inhibition percentages at a 30-minute exposure duration (I30), with a reference to a control solution consisting of a stock saline solution.

3. Results and discussion

3.1. Morphological characterization

The morphology and particle size of the coupled semiconductors were analyzed by TEM (Fig. 2). Rod-like nanoparticles of an average length of 26 nm were observed for pure TiO$_2$ nanoparticles, Ti100 (Fig. 2**a**). Spherical-shaped and smaller nanoparticles appear by adding Zr in the nanoparticle formulation. A mixture of rod-like and spherical-shaped nanoparticles is obtained for Ti70Zr30 sample (Fig. 2**b**) whereas just spherical-shaped nanoparticles are observed at Zr contents higher than 30 % (Fig. 2**d–f**). The higher the Zr content the lower the particle size and narrower pore size distributions are obtained (Fig. 2**h**). The average particle size (Table 1) decreases from 26 nm for Ti100 to 3.4 for Ti30Zr70, and then increases to 4.9 nm for pure Zr100. TEM mapping was performed on the Ti70Zr30 sample in order to analyze the Ti and Zr distribution on the nanoparticle surface (Fig. 2**g**). As it was expected, Ti is the major component of the particles and Zr is homogeneously distributed along the nanoparticles surface.

3.2. XRD

The crystallinity of nanoparticles was analyzed by XRD. Fig. 3 displays the diffractograms, while Table 1 presents the particle size and d-spacing values obtained by applying the Scherrer equation and the Bragg law, respectively, to the most intense diffraction peak. Note that the crystallite size obtained by XRD is higher than the particle size obtained by TEM (Table 1) at low Ti contents, because these samples are formed mainly by particles of size lower than 5 nm and analyzing crystalline domain sizes below 5 nm using XRD, is challenging due to both broad peaks and low signal-to-noise ratios. In this sense, only the biggest particles are detected by XRD. At high Ti contents, TEM and XRD
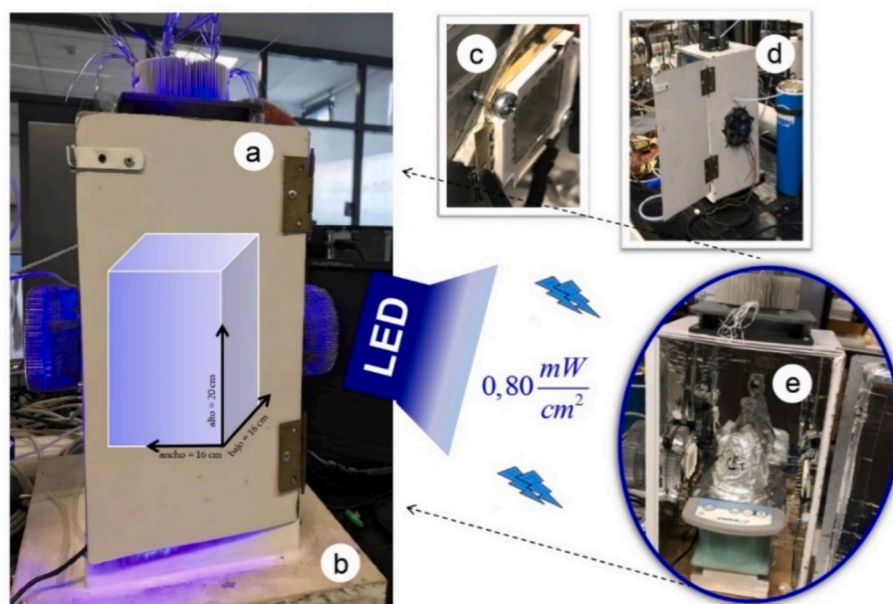

Fig. 1. Photocatalytic batch reactor. (a) The upper part contains the reaction medium LED lamps, (b) the lower part contains the power sources, (c) LED lamp (d) Side fan to promote cooling, and (e) a 250 mL borosilicate glass reactor.
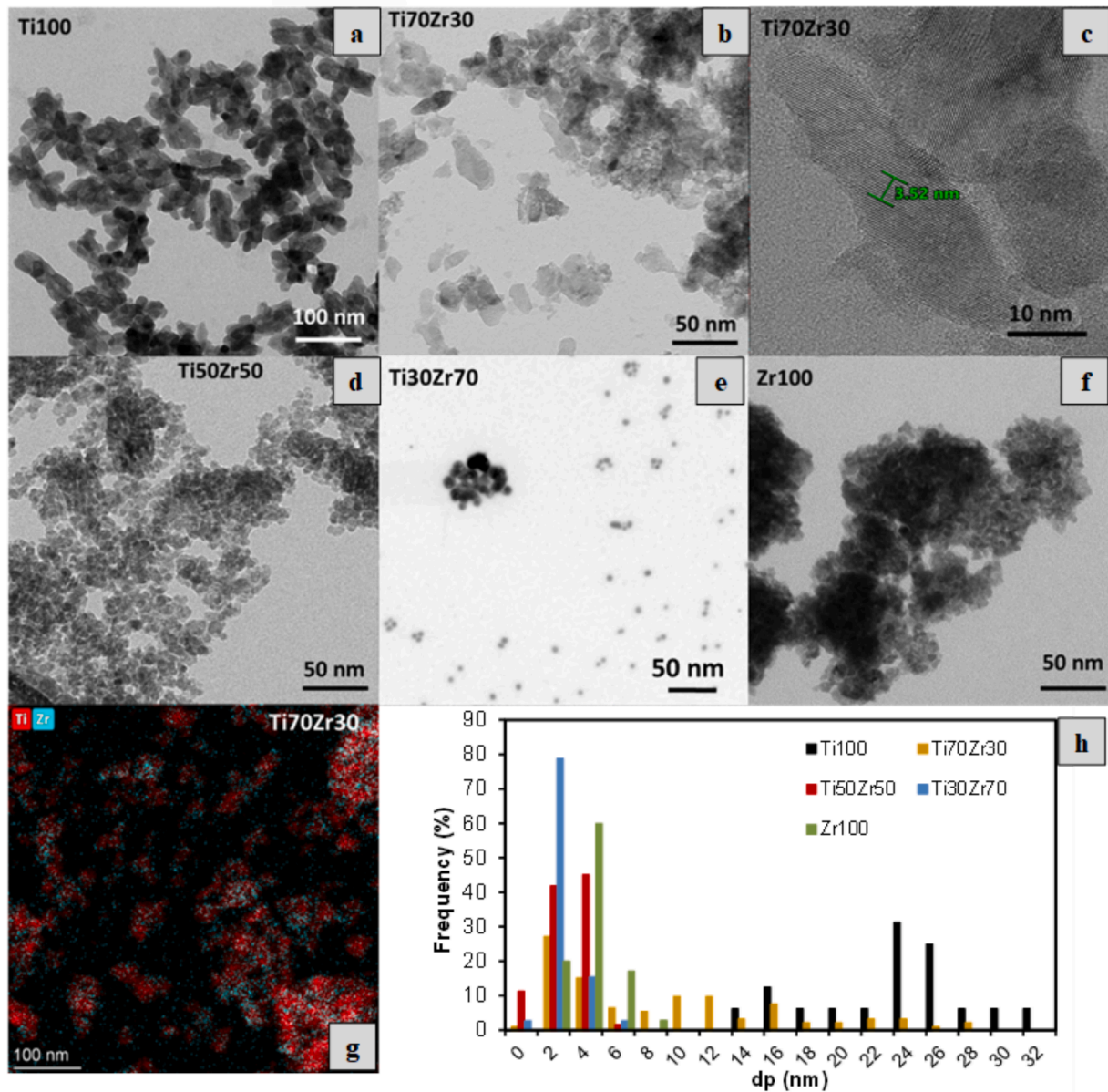
Fig. 2. **(a–f)** TEM images, **(g)** TEM mapping, and **(h)** particle size distributions of pure (Ti100 and Zr100) and mixed (TiXZrY) oxides nanoparticles.

Table 1
Results from the characterization of the catalysts through N_2 adsorption and XRD.

Sample	N_2-isotherm			XRD		TEM
	S_{BET}	$V_{0.95}$	V_{MESO}	dp	d-spacing	dp
	$m^2\ g^{-1}$	$cm^3\ g^{-1}$		nm	nm	nm
Zr100	101	0.124	0.082	8.5	0.2949	4.9
Ti10Zr90	171	0.134	0.080	n.a.	0.2951	–
Ti30Zr70	190	0.101	0.043	n.a.	n.a.	3.4
Ti50Zr50	182	0.180	0.103	10.6	0.3531	3.8
Ti70Zr30	165	0.248	0.194	10.1	0.3517	11.2
Ti100	78	0.216	0.082	10.8	0.3252	26.0
Ti-com	17	0.019	0.015	28.8	0.3523	–

S_{BET}: BET surface area, dp (XRD): crystallite size determined by Scherrer equations.

particle sizes are similar, since size distributions are centered at higher sizes. It is important to highlight that no diffraction peaks are obtained for Ti30Zr50 sample, since particles with sizes lower than 4 nm are obtained, as it was observed from TEM images (Fig. 2**h**).

On the other hand, the anatase phase is detected in commercial titania, whereas the rutile phase is stabilized in Ti100 nanoparticles. Moreover, peaks become wider in the Ti100 sample regarding Ti-com, denoting a smaller particle size (10.8 nm vs 28.8 nm, Table 1). The d-spacing was 0.3252 nm for Ti100 and 0.3523 nm for Ti-com which aligns well with the (1 1 0) and (1 0 1) crystallographic planes of rutile and anatase TiO_2, respectively [41]. TiO_2 physicochemical properties are deeply affected by the crystal structure. Rutile TiO_2 exhibits a narrower bandgap, greater dielectric constant, and higher refractive index compared to anatase TiO_2, all of which are favorable attributes for various photonic applications. The rutile phase can be obtained from methods that favor the direct precipitation of TiO_2 from a liquid phase, such as hydrothermal methods. Aside from this method, rutile is just obtained through anatase phase thermal transition [42,43]. However the transformation from anatase to rutile phase typically requires elevated temperatures, often ranging from 600 to 800 °C [44,45]. The average crystal size seems to be a crucial factor, affecting the anatase to rutile transformation [43,46–48]. Anatase exhibits the highest
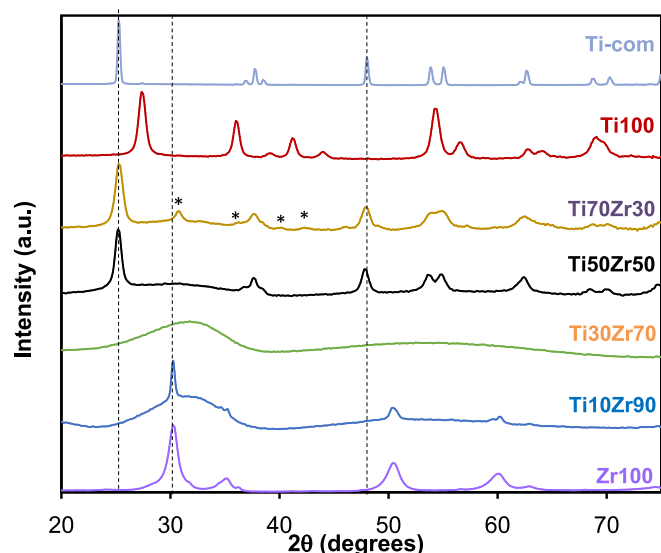
Fig. 3. XRD patterns of TiXZrY nanoparticles.

Fig. 4. N_2 adsorption–desorption isotherms of TiXZrY samples.

thermodynamic stability at sizes smaller than 11 nm, while brookite prevails for crystal sizes ranging from 11 to 35 nm. Rutile, on the other hand, is most stable when crystal sizes exceed 35 nm [46,49]. Thus, anatase can be synthesized at ultrafine sizes [49]. However, nanosized TiO_2 could transform to rutile by heating, and this transition temperature is affected by the initial particle size. Li *et al.* [47] observed that the lowest transition starting temperature and thermal stability was obtained with 12 nm anatase, compared with 17 and 23 nm samples. Here, TiO_2 nanoparticles of an average crystallite size of 10.8 nm were obtained in Ti100 after a calcination at 400 °C. A priori, at this crystal size, anatase phase could be expected rather than a rutile one. Moreover, the calcination temperature is low enough to produce an anatase to rutile transformation. However, the ultrafine TiO_2 particles obtained by the two-emulsion method, could decrease the transformation temperature since size affects the number of particle–particle contacts within a given volume, favoring the phase transition and consequently the stabilization of small rutile nanoparticles.

The incorporation of Zr to the titania formulation, changes the diffraction pattern in comparison with Ti100. Ti70Zr30 shows a diffraction pattern similar to anatase TiO_2 but new peaks emerge at 30.8°, 35.9°, 40.9° and 42.1° which could be identified as zirconium titanates, $Ti_{0.33}Zr_{0.67}O_2$ (JCPDS 46-1265) [50,51] and $ZrTiO_4$ (34-0415) [52]. These peaks almost disappear by increasing the Zr content. For high Zr contents (>50 %), the zirconia cubic phase (JCPDS 49-1642) is the main crystalline structure detected. In these cases, the monoclinic zirconia phase could be expected, since the stable phase is at temperatures below 1200 °C, whereas tetragonal and cubic phases are stable at temperatures above 1200 and 2400 °C, respectively [53]. However, the zirconia phase stabilization is also size-dependent. Consequently, the cubic phase can be stabilized at a crystallite size lower than 11 nm [54]. A crystallite size of 8.5 nm was obtained for Zr100 which could explain the stabilization of the cubic phase. The d-spacing corroborates that the anatase phase predominates for samples with high Ti content (≥50 %) whereas the zirconia cubic phase with a d-spacing of 0.295 nm is predominant at higher content of Zr (>50 %) [55].

3.3. N_2-isotherms

The porous structure of the samples was examined through N_2 adsorption–desorption analysis and results are collected in Fig. 4 and Table 1. Type II isotherm is obtained for Ti100 typical of microporous materials whereas hybrid type I-IV isotherms were observed for the TiXZrY samples, exhibiting a distinct hysteresis loop that indicates the
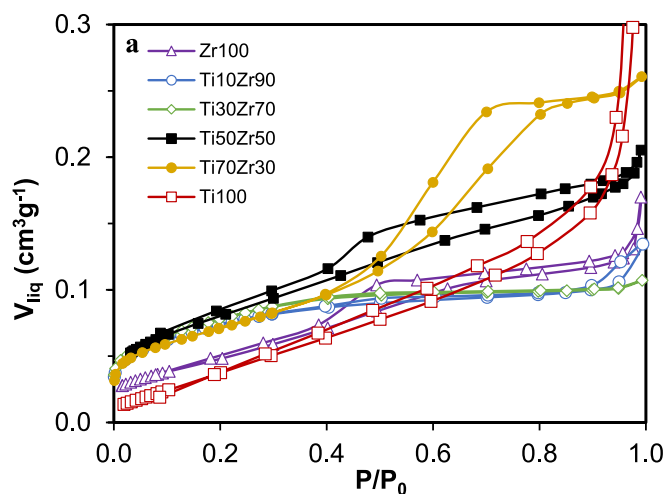
presence of mesopores. The N_2 adsorption at low pressures is likely related to adsorption on the external surface of the nanoparticles, while the presence of mesopores can be attributed to interparticle voids. Note that the surface area (S_{BET}) is directly related to the nanoparticle size. The lower the d_p (TEM) the higher the S_{BET}, that is, nanoparticles expose more external surface-per-volume. The N_2-adsorption at higher relative pressures and the hysteresis loop also depend on the Zr content and, consequently, the particle size. Interparticle voids left by the big particles (26 nm) of Ti100, should be in the range of wide mesopores or macropores which explains the fast N_2-uptake at P/P_0 close to 1. As it was observed by TEM, the addition of Zr decreases the particle size below 11 nm, and consequently, narrower interparticle voids are left, increasing the N_2-adsorption at moderate relative pressures proper of mesoporous materials. This N_2-adsorption at moderate relative pressures and the hysteresis loop, decreases by increasing the Zr content due to the particle size decrease up to almost disappearing at high Zr contents (Ti30Zr70, Ti10Zr90, and even Zr100), denoting that the interparticle voids left by these small particles (<4 nm) are in the micropores range.

3.4. Band gap

The band gap (E_g) of the prepared photocatalysts was studied by diffuse reflectance spectroscopy. The band gap of samples can be evaluated using the Kubelka–Munk function, F(R). The E_g value could be obtained by plotting $(F(R)E)^n$ as a function of E (hν). A value of n = 1/2 was considered for permitted direct transitions. The Kubelka Munk plot of samples is presented in Fig. 5 and the obtained E_g is collected in Table 2. The E_g value obtained for Ti-commercial was 3.22 eV which closely aligns with the reported value for the titania anatase phase (3.20 eV) [56,57]. The E_g decreases to 2.98 eV for Ti100 nanoparticles which can be attributed to the stabilization of the rutile phase showing a reported band gap of 3.0 eV [57]. For pure ZrO_2 samples (Fig. 5b), the band gap decreases from 5.0 eV to 4.5 eV for monoclinic Zr-com and cubic Zr100. The TiO_2/ZrO_2 heterojunction decreases the band gap of samples. The higher the content of Ti, the lower the band gap of the TiXZrY photocatalysts, achieving the optimal value with a content of Ti of 50–70 %. This red shift of the optical absorption edge of the material, could be explained by the Ti doping of bulk ZrO_2. Gallino *et al.* [58] demonstrated that the introduction of Ti into bulk ZrO_2, results in the creation of an unoccupied Ti_{3d} band, positioned approximately 0.5 eV below the bottom of the conduction band which induces a decrease of the band gap. Consequently, the inclusion of ZrO_2 into TiO_2 results in intermediate band gap values between the parent oxides (TiO_2 and ZrO_2). However, it's worth noting that an unconventional decrease in
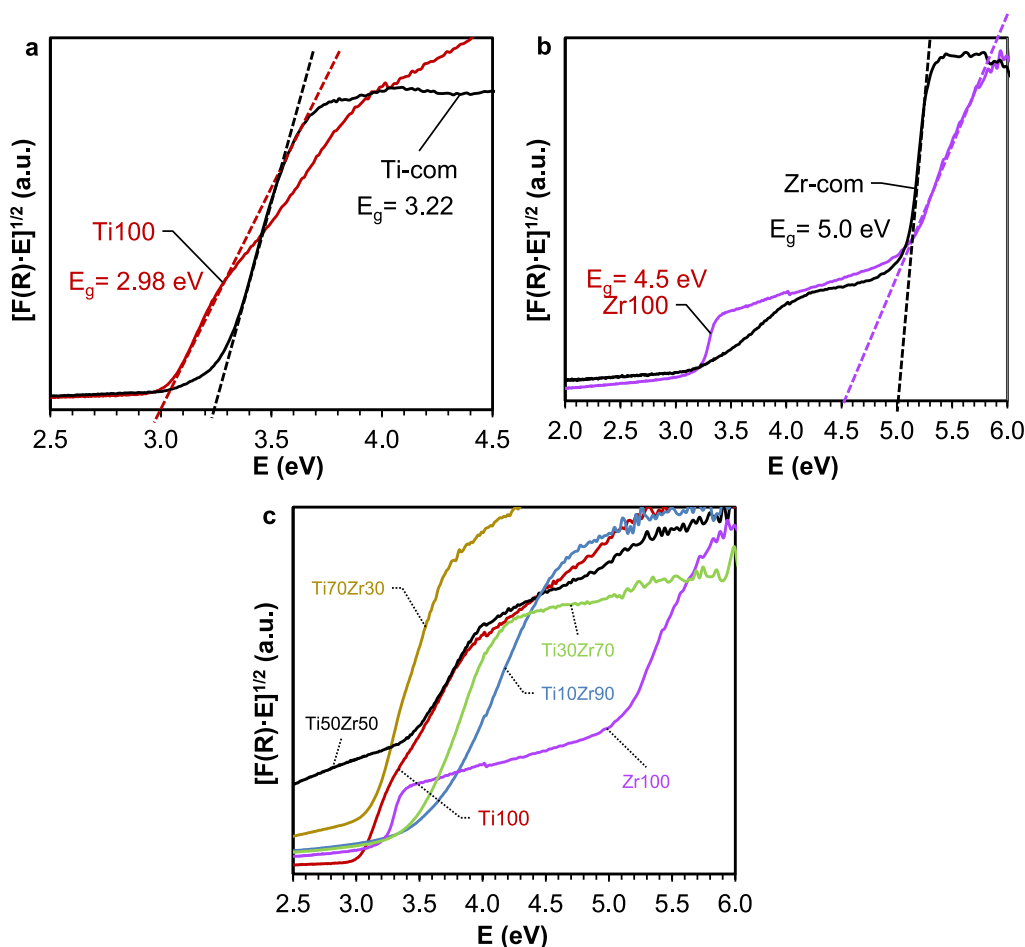
Fig. 5. Diffuse reflectance spectra of a) pure TiO_2 samples, b) pure ZrO_2 samples, and c) TiXZrY nanoparticles.

Table 2
Band gap.

Sample	Band-Gap
Zr100	4.55
Ti10Zr90	3.42
Ti30Zr70	3.32
Ti50Zr50	2.82
Ti70Zr30	2.90
Ti100	2.98

band gap values was observed when Zr was incorporated into TiO_2 (Ti50Zr50 and Ti70Zr30) samples due to the formation of zirconium titanates phases (see XRD plot). The creation of a heterojunction between the zirconium titanate phases and the titania anatase phase, can be attributed to the reduction in band gap values [59,60].

3.5. XPS

The surface chemistry of the samples was analyzed by XPS. C_{1s}, O_{1s}, Ti_{2p}, and Zr_{3d} spectral regions are depicted in Fig. 6, and data obtained from their deconvolutions are collected in Table S1. Adventitious carbon was used as a reference for the calibration of the binding energies. There is evidence suggesting that CO or CO_2 species may be involved in the gradual accumulation of carbon on pristine oxide surfaces [61]. Oxygen vacancies can significantly impact the interaction between the surface and CO_2, thereby increasing the adsorption of CO_2 molecules and leading to the formation of carbon intermediates [62–66]. Oxygen vacancies formed on the surface of titania are directly involved in the

activation of CO_2, resulting in the formation of carbonate species. Thus, the amount of carbon fixed could be related to the exposed surface of the material and its surface chemistry. Three peaks were necessary to accurately model the C_{1s} spectral region at 284.6, 285.8, and 288.5 eV identified as C–C, C-O, and COO^-. The carbon content (C_{1s}, Table S1) seems to depend on the surface area of the materials. The lower the particle size, the more exposed the defect-rich surface, and the higher the adventitious carbon fixed. Note also that carbonate species are present in nanoparticles where they are not detected in Ti-com, probably indicating a more oxygen vacancies concentration on the nanoparticles surface. The amount of carbonate (COO^-) increases in the mixed oxides, is probably due to the heterojunction of Ti-Zr which creates a more oxygen-deficient structure. The presence of these oxygen vacancies can be also observed by analyzing de O_{1s} region (Fig. 6b). Three peaks are also observed in the O_{1s} region at 529.8, 531.1, and 532.5 eV assigned to lattice oxygen (O_L), adsorbed oxygen on the vacancies (O_{ads}), and C-O species, respectively [21,67]. The O_{ads} component of TiXZrY samples is much higher than that of the pure Ti samples, denoting a more oxygen-vacancies-rich surface as was pointed out from the C_{1s} region.

For pure TiO_2 samples (Ti100 and Ti-com), the $Ti_{2p3/2}$ region (Fig. 6c) was deconvolved in one peak, centered at around 430.0 eV attributed to Ti^{4+}. A new peak appears at 458.2 eV for Ti_XZr_Y samples which can be ascribed to Ti^{3+}/zirconium titanates species [20,68]. The same conclusions can be obtained by analyzing the $Zr_{3d5/2}$ region (Fig. 6d). For pure ZrO_2 (Zr100), two peaks appear at 181.6 eV and 182.6 eV which are ascribed to Zr^{+4} in stoichiometric ZrO_2 and non-stoichiometric oxides (ZrOy: $0 < y < 2$), respectively [20]. Two peaks, which are shifted 0.8 eV to higher B.E, were also required to deconvolve the $Zr_{3d5/2}$ region for TiXZrY samples, but the relative intensity of both

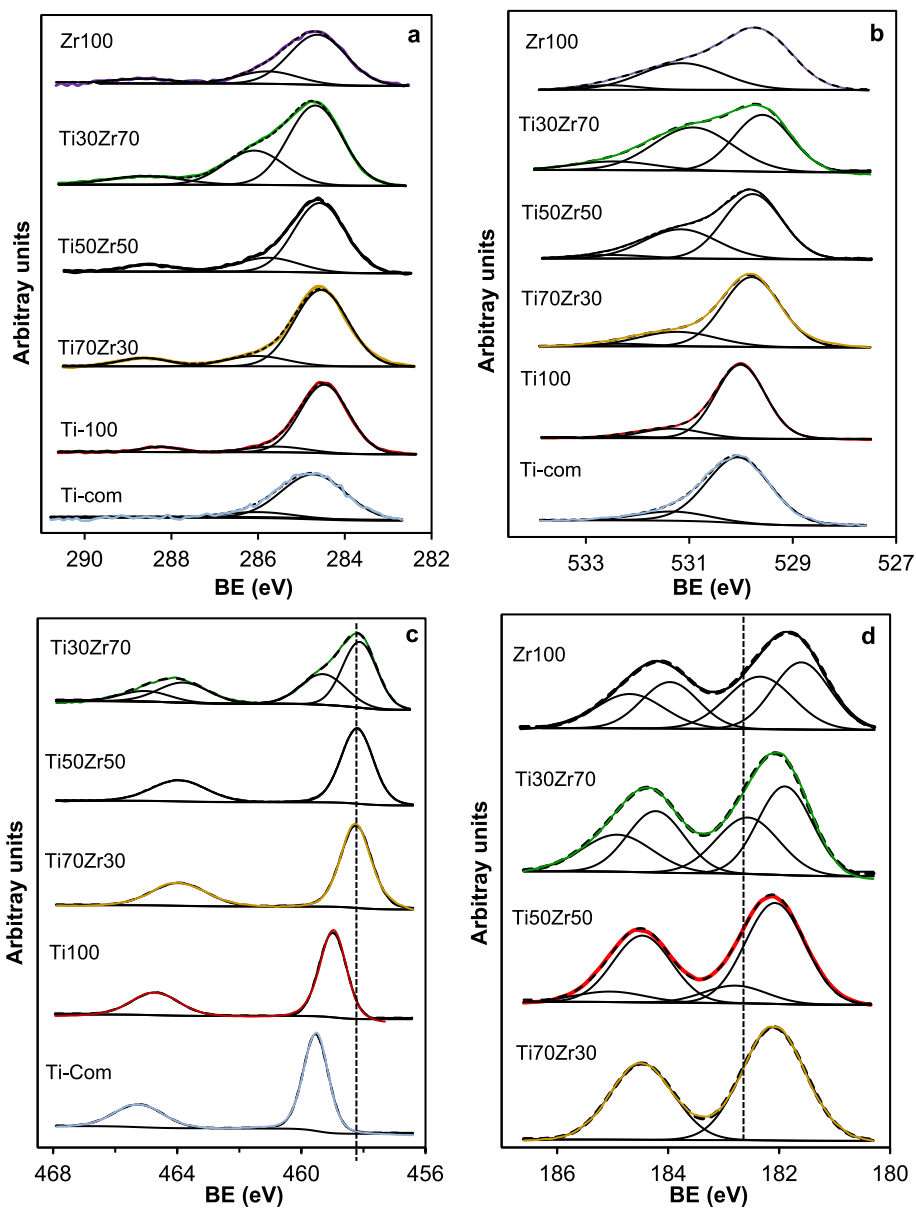**Fig. 6.** XPS spectra: a) C_{1s}, b) O_{1s}, c) Ti_{2p}, and d) Zr_{3d}. Experimental data: coloured line; Deconvolved peaks: black thin line; Resulted fitting: dashed line.
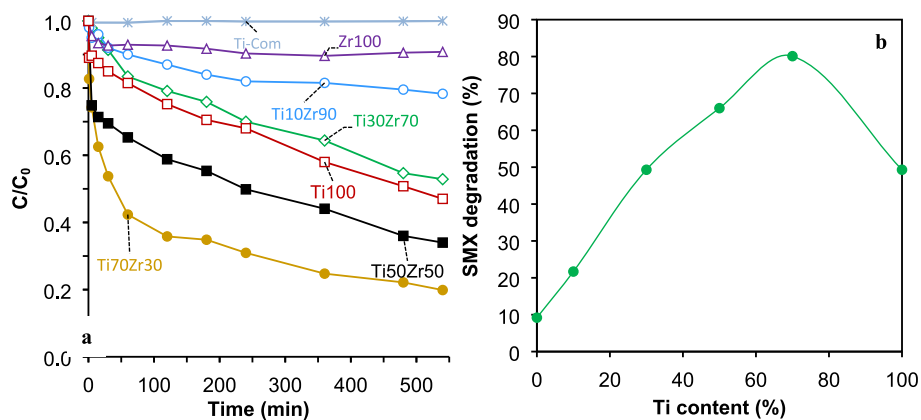

Fig. 7. A) Kinetics of photocatalytic degradation of TiXZrY samples under Blue-LED irradiation. **b)** % of SMX degradation achieved at 540 min as a function of the Ti content in the TiXZrY samples.

peaks is different, depending on the Ti content. The peak at 181.7 eV can be attributed to the $Zr_{3d3/2}$ in hybridized ZrO_2–TiO_2 nanostructure, whereas the peak at 182.6 eV can be attributed to $Zr_{3d3/2}$ in free ZrO_2. It is important to highlight that the contribution of this hybridized ZrO_2–TiO_2 peak was 100, 84.4 and 49.9 % for Ti70Zr30 (stoichiometric hybridized ZrO_2–TiO_2), Ti50Zr50 and Ti30Zr70, respectively which is in good agreement with the main contribution of the 458.2 eV $Ti_{2p3/2}$ signal in Ti70Zr30 and Ti50Zr50 samples ascribed to Ti^{3+}/zirconium titanates species. Thus, the hybridized ZrO_2–TiO_2 nanostructure seems to increase with the Ti content in accordance with the XRD results to be maximum for the Ti70Zr30 (stoichiometric zirconium titanate).

3.6. Photocatalytic tests

The synthesized catalysts were tested in the degradation of SMX using blue-LED irradiation (465 nm). For that, the nanoparticles were previously saturated in the dark with a solution of the proper concentration to achieve a final concentration of 5 mg/L. The SMX photo-degradation kinetics of all samples are plotted in Fig. 7.

From Fig. 7**a**, it can be observed that Ti-com is not photoactive because the energy of the blue LED is not enough to promote an electron from the valence band to the conduction band, which is caused by the wide band gap. However, the miniaturization of titania size in Ti100 increases the photoactivity to 49.3 %, despite the less photoactive crystal phase (rutile) being obtained. Conversely, the Zr100 sample is poorly active due to the high band gap of the sample. The activity increases by adding Ti to the sample which could be explained based on the decrease of the band gap and the decrease of the particle size. The decrease of the particle size enhances the photocatalytic performance due to i) the increase of the photo-catalytically active surface area for the degradation of SMX and ii) the minimization of the distance that photogenerated electrons and holes need to cross to reach the surface where the reaction occurs, and consequently, the minimization of the electron-hole recombination probability. Note that by only adding 30 % of Ti to the Zr nanoparticle composition the degradation activity achieved (49.3 %) is similar to the obtained for Ti100 (53 %). However, a synergistic effect is obtained for nanoparticles with a 50 % and 70 % of Ti. If segregated phases were obtained, a dilution effect would be expected by increasing the Ti content, and an average activity between the obtained for Ti-100 and Zr-100 would be obtained for the Ti50Zr50
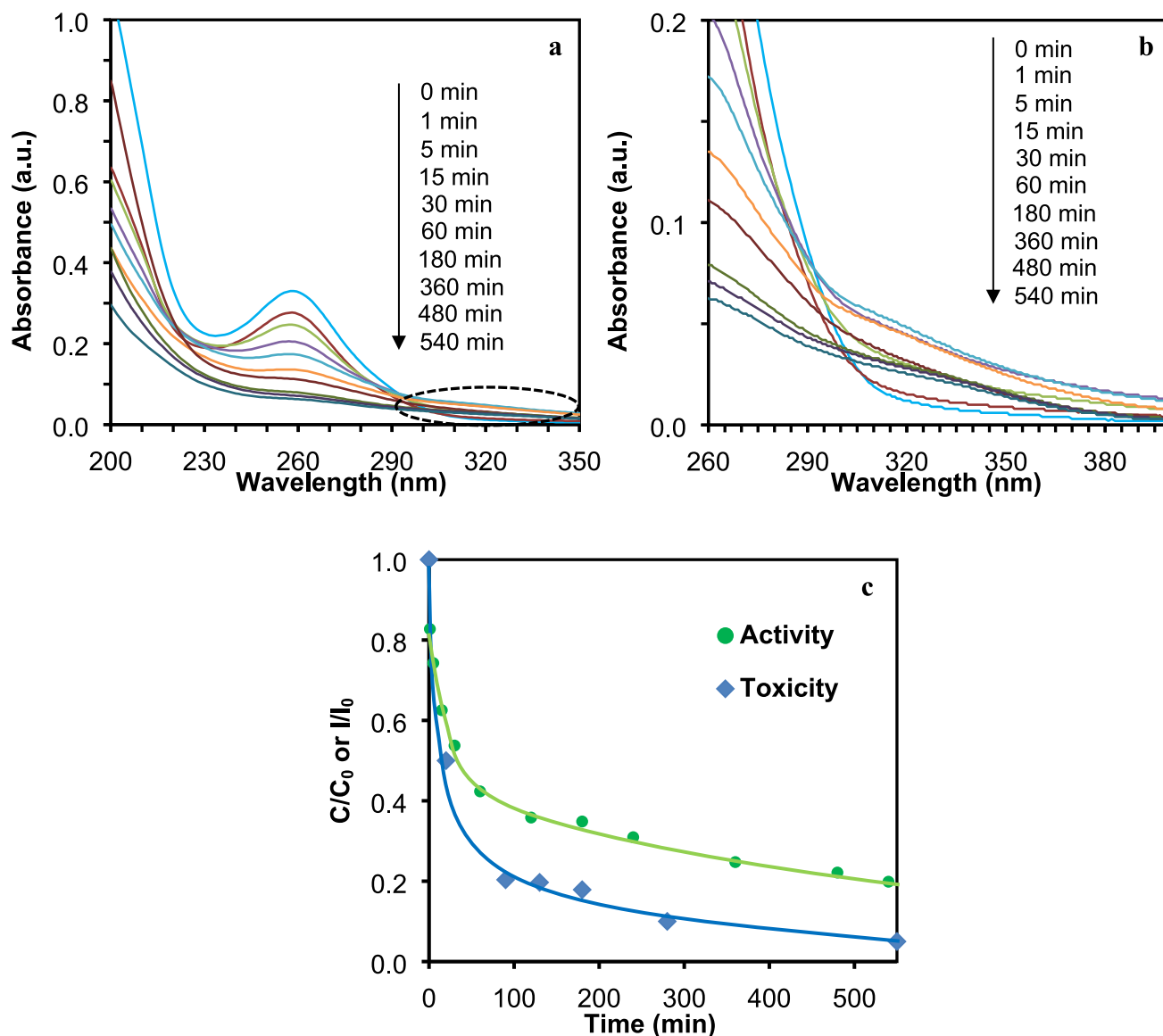

Fig. 8. (a–b) Absorption spectra of the SMX solutions with different degradation times under Blue-LED irradiation and c) variation of the toxicity of solution treated for Ti70Zr30.

sample. However, the activity highly increases from 53 % (Ti100) to 66 % for Ti50Zr50 which could be explained based on, as commented, the active surface area increasing along with the reduction in the band gap. However, a SMX degradation percent as high as 80.1 % was obtained for Ti70Zr30 under blue-LED irradiation, although the surface area has decreased, and the band gap has increased in this sample, compared to the Ti50Zr50 one. This activity enhancement is explained, based on the formation of zirconium titanates observed by XRD and XPS. The heterojunction comprising $ZrTiO_4/ZrTi_2O_6/TiO_2$ extends the lifespan of photogenerated charge carriers, thereby enhancing photoactivity. [20,68] Briefly, the optimal SMX degradation (Fig. 7b) in sample Ti70Zr30 is achieved due to an optimal combination of surface area, band gap, and formation of hybridized zirconium titanates nanostructured.

SMX exhibits a UV–visible absorption spectrum characterized by a solitary peak, which reaches its maximum absorption at 258 nm. This distinctive peak can be attributed to a π–π* transition, most likely associated with the aniline group. UV–visible absorption spectroscopy was employed to assess the extent of transformation induced in SMX. Fig. 8a illustrates a notable reduction in the distinctive absorption peak of SMX for the Ti70Zr30 sample over varying irradiation periods ranging from 0 to 540 min. This decline ultimately means the complete disappearance of the SMX absorption band. It's worth mentioning that a rise in absorbance within the wavelength range of 300–450 nm in the spectrum, indicates the generation of byproducts [69,70]. The emergence of a new absorption band at 250 nm can be also ascribed to the

degradation of SMX leading to the formation of byproducts. This occurrence suggests that the phenyl and pyrimidine bands have not entirely disappeared, as some remnants of their structure persist in the degradation byproducts, notably the C-N and C=N bonds.[71] Analyzing Fig. 8a–b, the appearance of a new band at 250 nm is not observed and only a slight increase of absorption in the 300–400 range is observed for Ti70Zr30 low irradiation times (<60 min) which then decreases at longer irradiation times. This could indicate the generation of some byproducts at low irradiation times which are then degraded or, probably, completely mineralize.

The toxicity of the treated water using Ti70Zr30 sample as photocatalyst was also studied, using the normalized biotest of luminescent inhibition of *Vibrio fischeri* bacteria. Data are plotted in Fig. 8c. Note that the toxicity of the water decreases, showing a closed behavior to the activity curve for the same irradiation times. This fact indicates that SMX is completely mineralized, reducing simultaneously the toxicity of the treated water, or the generated new byproducts are less toxic than the pristine SMX.

Bibliographic results using materials with similar nature (ZrO₂-TiO₂ composites) were recorded in Table 3 despite we rarely found Ti-Zr nanoparticles applied in drug degradation in water media. It is observed that in most of the cases found, UV irradiation is required to obtain a high drug or dye degradation. In the present work, visible light is used obtaining high degradation percent which is comparable with the bibliographic data using a less powerful light source (λ = 465 nm).

Table 3

Comparison of the behavior of different Ti/Zr materials for photocatalytic degradation of dyes and drugs in water from literature.

Nature of Sample	Nomenclature and optimum sample	Synthesis method	Organic Pollutant	Experimental conditions		Photocatalytic efficiency	
				Mass of catalyst, volume, initial drug concentration, pH (mg; mL; mg/L)	Source Illumination (W)	Degradation; time (%; min)	Ref.
TiO₂/ZrO₂- CMCS (carboxymethyl chitosan)	**T/Z-x** x = content of titanium (%) (nTi:nZr = x:100) obtained by calcining T/Z-CMCS-x at 600 °C. **T/Z-5**	Microwave solvothermal	Rhodamine B	50; 100; 10; 10.3	UV-Light (CEL-LPH120)	90.5; 270	[72]
TiO₂/ZrO₂	**TMZ-x** (x = a, b, c, d, e) x = Zr/Ti molar ratio (3, 6, 9, 12, 15) **TMZ-b** Zr/Ti = 6 %	Hybrid sol–gel	Azo-dye, Ponceau BS	180; 180; 0.1 mM; Not shown	Medium pressure mercury lamp (125 W Philips)	99.3; 27	[73]
TiO₂/ZrO₂	**TiO₂-ZrO₂ x:y** x:y = Ti:Zr % **TiO₂-ZrO₂ 95:5**	Sol-gel	Metformin	500; 500; 10; 8	Mercury lamp (125 W)	70;180	[74]
TiO₂/ZrO₂ derived from zirconium MOF	**TiO₂/UiO-66**	Solvothermal	Rhodamine B	160; 200; 20; 9	LED lamp (100 w)	99; 180	[75]
Mesoporous TiO₂/ ZrO₂	**sTiZrx-T** Where s, x and T represents sol–gel method, mol% of Zr and calcination temperature. **sTiZr0.05–700**	Sol-gel	Chloridazon	150; 50; 11; Not shown	Xenon lamp (150 W)	~55; 300	[76]
N-doped TiO₂/ZrO₂ derived from Ti/Zr MOFs	**N-TiO₂-ZrO₂-x** x = content of zirconium (%) **N-TiO₂-ZrO₂-5**	Hidrotermal	Methylene blue Tetracycline Phenol	10; 100; 20: Not shown	UV Lamp (500 W)	93.2; 80 86.3; 120 72.4; 120	[77]
Zr/TiO₂	**x mol.% Zr/TiO₂** x = content of zirconium (%) 2 mol % Zr/TiO₂	Thermal hydrolysis	Acid orange 7	50; 150; 3 × 10⁻⁵ mol/L; Not shown	UV Lamp (36 W)	99; 180	[78]
TiO₂/ZrO₂ NPs	**TixZry** x and y wt. % of TiO₂ and ZrO₂, respectively **Ti70Zr30**	Inverse microemulsion	sulfamethoxazole	100; 100; 5; 7	Blue LED lamp (100 W)	80.1; 540	This work

4. Conclusions

TiO$_2$-ZrO$_2$ hybrid photocatalysts (TiXZrY) were prepared, using a reversed microemulsion method, and efficiently tested in the degradation of sulfamethoxazole (SMX) in water under blue-LED irradiation. TEM images reveal that as the Zr content increases, the particle size decreases, obtaining narrower pore size distributions. The average particle size decreases from 26 nm and 4.9 nm for pure TiO$_2$ (Ti100) and ZrO$_2$ (Zr100), respectively to 3.4 nm for Ti30Zr70. The smaller the dp (determined by TEM), the greater the S$_{BET}$ (specific surface area) becomes, indicating that nanoparticles expose a higher external surface area per unit volume. XRD findings reveal that at a low Zr content (Ti70Zr30, Ti50Zr50), zirconium titanates are formed, while at higher Zr concentrations (ZrO$_2$ > 50 wt%), the predominant crystalline structure detected is cubic zirconia, despite monoclinic zirconia being the stable phase at temperatures below 1200 °C. The band gap decreases up to E$_g$ = 2.8 eV by increasing the ZrO$_2$ content up to 50 % which can likely be attributed to the creation of a heterojunction between the zirconium titanate phases and the titania anatase phase.

Under blue-LED irradiation, the Ti70Zr30 photocatalyst achieved an impressive SMX degradation rate of up to 80.1 %, accompanied by a decrease in the toxicity of the treated water. This result can be attributed to the formation of zirconium titanates, as observed through XRD and XPS analyses, as well as the presence of a high active surface area.

CRediT authorship contribution statement

Jhon Mauricio Aguirre-Cortés: Methodology, Investigation, Formal analysis. **Álvaro Munguía-Ubierna:** Investigation, Data curation. **Adriana Moral-Rodríguez:** Methodology, Investigation, Formal analysis, Data curation. **A.F. Pérez-Cadenas:** Visualization, Validation, Supervision, Project administration. **F. Carrasco-Marín:** Visualization, Validation, Supervision. **E. Bailón-García:** Writing – review & editing, Writing – original draft, Validation, Supervision, Funding acquisition, Formal analysis, Conceptualization.

Declaration of competing interest

The authors declare that they have no known competing financial interests or personal relationships that could have appeared to influence the work reported in this paper.

Data availability

Data will be made available on request.

Acknowledgments

Appendix A. Supplementary material

Supplementary material to this article can be found online at https://doi.org/10.1016/j.apsusc.2024.160609.

References

[1] J.P. García-Cambero, H. García-Cortés, Y. Valcárcel, M. Catalá, Environmental concentrations of the cocaine metabolite benzoylecgonine induced sublethal toxicity in the development of plants but not in a zebrafish embryo-larval model, J. Hazard. Mater. 300 (2015) 866–872, https://doi.org/10.1016/j.jhazmat.2015.08.019.

[2] K.A. Kidd, P.J. Blanchfield, K.H. Mills, V.P. Palace, R.E. Evans, J.M. Lazorchak, R.W. Flick, Collapse of a fish population after exposure to a synthetic estrogen, Proc. Natl. Acad. Sci. U. S. A. 104 (2007) 8897–8901, https://doi.org/10.1073/pnas.0609568104.

[3] N. Osazee, I. Tongo, L. Ikechukwu, Ecotoxicology and Environmental Safety Acute effects of acetaminophen on the developmental, swimming performance and cardiovascular activities of the African catfish embryos / larvae (Clarias gariepinus), Ecotoxicol. Environ. Saf. 208 (2021) 111482, https://doi.org/10.1016/j.ecoenv.2020.111482.

[4] M. Akiba, T. Sekizuka, A. Yamashita, M. Kuroda, Y. Fujii, M. Murata, K.I. Lee, D.I. Joshua, K. Balakrishna, I. Bairy, K. Subramanian, P. Krishnan, N. Munuswamy, R.K. Sinha, T. Iwata, M. Kusumoto, K.S. Guruge, Distribution and relationships of antimicrobial resistance determinants among extended-spectrum-cephalosporin-resistant or carbapenem-resistant Escherichia coli isolates from rivers and sewage treatment plants in India, Antimicrob. Agents Chemother. 60 (2016) 2972–2980, https://doi.org/10.1128/AAC.01950-15.

[5] J. Zhou, X. Yun, J. Wang, Q. Li, Y. Wang, A review on the ecotoxicological effect of sulphonamides on aquatic organisms, Toxicol. Reports. 9 (2022) 534–540, https://doi.org/10.1016/j.toxrep.2022.03.034.

[6] L.H.M.L.M. Santos, A.N. Araújo, A. Fachini, A. Pena, C. Delerue-Matos, M.C.B.S.M. Montenegro, Ecotoxicological aspects related to the presence of pharmaceuticals in the aquatic environment, J. Hazard. Mater. 175 (2010) 45–95, https://doi.org/10.1016/j.jhazmat.2009.10.100.

[7] Z. Yan, Q. Yang, W. Jiang, J. Lu, Z. Xiang, R. Guo, J. Chen, Integrated toxic evaluation of sulfamethazine on zebrafish: Including two lifespan stages (embryo-larval and adult) and three exposure periods (exposure, post-exposure and re-exposure), Chemosphere 195 (2018) 784–792, https://doi.org/10.1016/j.chemosphere.2017.12.119.

[8] D. Sinthuchai, S.K. Boontanon, N. Boontanon, C. Polprasert, Evaluation of removal efficiency of human antibiotics in wastewater treatment plants in Bangkok, Thailand Water Sci. Technol. 73 (2016) 182–191, https://doi.org/10.2166/wst.2015.484.

[9] D. Xu, Y. Xie, J. Li, Ecotoxicology and Environmental Safety Toxic effects and molecular mechanisms of sulfamethoxazole on Scenedesmus obliquus, Ecotoxicol. Environ. Saf. 232 (2022) 113258, https://doi.org/10.1016/j.ecoenv.2022.113258.

[10] E. Sanganyado, Policies and regulations for emerging pollutants in freshwater: Challenges and opportunities, Emerg. Freshw. Pollut. (2022), https://doi.org/10.1016/B978-0-12-822850-0.00007-7.

[11] E. Antunes, A.K. Vuppaladadiyam, A.K. Sarmah, Application of biochar for emerging contaminant mitigation, 1st ed., Elsevier Inc., 2021. doi: 10.1016/bs.apmp.2021.08.003.

[12] P.S. Basavarajappa, S.B. Patil, N. Ganganagappa, K.R. Reddy, A.V. Raghu, C.V. Reddy, ScienceDirect Recent progress in metal-doped TiO$_2$, non-metal doped/codoped TiO$_2$ and TiO$_2$ nanostructured hybrids for enhanced photocatalysis, Int. J. Hydrogen Energy. 45 (2020) 7764–7778, https://doi.org/10.1016/j.ijhydene.2019.07.241.

[13] J.C. Colmenares, M.A. Aramendía, A. Marinas, J.M. Marinas, F.J. Urbano, Synthesis, characterization and photocatalytic activity of different metal-doped titania systems, Appl. Catal. A Gen. 306 (2006) 120–127, https://doi.org/10.1016/j.apcata.2006.03.046.

[14] M. Sadia, R. Naz, J. Khan, M. Zahoor, R. Ullah, R. Khan, S. Naz, H.S. Almoallim, S. Ali, Journal of King Saud University – Science Metal doped titania nanoparticles as efficient photocatalyst for dyes degradation, J. King Saud Univ. - Sci. 33 (2021) 101312, https://doi.org/10.1016/j.jksus.2020.101312.

[15] S.Z. Islam, S. Nagpure, D.Y. Kim, S.E. Rankin, Synthesis and catalytic applications of non-metal doped mesoporous Titania, Inorganics 5 (2017) 15, https://doi.org/10.3390/inorganics5010015.

[16] Y. Bessekhouad, D. Robert, J.V. Weber, Bi$_2$S$_3$/TiO$_2$ and CdS/TiO$_2$ heterojunctions as an available configuration for photocatalytic degradation of organic pollutant, J. Photochem. Photobiol. A Chem. 163 (2004) 569–580, https://doi.org/10.1016/j.jphotochem.2004.02.006.

[17] J.M. Chem, C. Wang, R.L. Thompson, P. Ohodnicki, C. Matranga, Size-dependent photocatalytic reduction of CO$_2$ with PbS quantum dot, J. Mater. Chem. 21 (2011) 13452–13457, https://doi.org/10.1039/c1jm12367j.

[18] S. Ding, X. Yin, X. Lu, Y. Wang, F. Huang, D. Wan, One-step high-temperature solvothermal synthesis of TiO$_2$/sulfide nanocomposite spheres and their solar visible-light applications, ACS Appl. Mater. Interf. 4 (2012) 306–311.

[19] G. Song, F. Xin, J. Chen, X. Yin, Applied Catalysis A : General Photocatalytic reduction of CO$_2$ in cyclohexanol on CdS – TiO$_2$ heterostructured photocatalyst, Appl. Catal., A, Gen. 473 (2014) 90–95, https://doi.org/10.1016/j.apcata.2013.12.035.

[20] H. Hamad, E. Bailón-García, A.F. Pérez-Cadenas, F.J. Maldonado-Hódar, F. Carrasco-Marín, ZrO$_2$-TiO$_2$/Carbon core-shell composites as highly efficient solar-driven photo-catalysts: an approach for removal of hazardous water pollutants, J. Environ. Chem. Eng. 8 (2020) 104350, https://doi.org/10.1016/j.jece.2020.104350.

[21] E. Bailón-García, A. Elmouwahidi, M.A. Álvarez, F. Carrasco-Marín, A.F. Pérez-Cadenas, F.J. Maldonado-Hódar, New carbon xerogel-TiO$_2$ composites with high

performance as visible-light photocatalysts for dye mineralization, Appl. Catal. B Environ. 201 (2017) 29–40, https://doi.org/10.1016/j.apcatb.2016.08.015.

[22] S. Benjedim, J. Castelo-Quibén, E. Bailón-García, E.M. Lotfi, A.F. Pérez-Cadenas, V. Slovák, J. Kalina, F. Carrasco-Marín, Activated carbon-based coloured titania nanoparticles with high visible radiation absorption and excellent photoactivity in the degradation of emerging drugs of wastewater, Carbon N. Y. 178 (2021) 753–766, https://doi.org/10.1016/j.carbon.2021.03.044.

[23] Y. Park, S.H. Lee, S.O. Kang, W. Choi, Organic dye-sensitized TiO$_2$ for the redox conversion of water pollutants under visible light, Chem. Commun. 46 (2010) 2477–2479, https://doi.org/10.1039/b924829c.

[24] S. Goulart, L.J. Jaramillo Nieves, A.G. Dal Bó, A.M. Bernardin, Sensitization of TiO$_2$ nanoparticles with natural dyes extracts for photocatalytic activity under visible light, Dye. Pigment. 182 (2020) 108654, https://doi.org/10.1016/j.dyepig.2020.108654.

[25] A.F. Nogueira, L.F.O. Furtado, A.L.B. Formiga, M. Nakamura, K. Araki, H.E. Toma, Sensitization of TiO$_2$ by supramolecules containing zinc porphyrins and ruthenium-polypyridyl complexes, Inorg. Chem. 43 (2004) 396–398, https://doi.org/10.1021/ic0345727.

[26] A. Islam, H. Sugihara, K. Hara, L.P. Singh, R. Katoh, M. Yanagida, Y. Takahashi, S. Murata, H. Arakawa, G. Fujihashi, Dye sensitization of nanocrystalline titanium dioxide with square planar platinum(II) diimine dithiolate complexes, Inorg. Chem. 40 (2001) 5371–5380, https://doi.org/10.1021/ic010391y.

[27] N. Jain, A. Mary, P.M. Dalal, R. Sakla, D.A. Jose, M. Jain, A.R. Naziruddin, Ruthenium complexes bearing bis-N-heterocyclic carbene donors in TiO$_2$ sensitization for dye-sensitized solar cells, Eur. J. Inorg. Chem. 2022 (2022), https://doi.org/10.1002/ejic.202200502.

[28] H. Kim, S. Jo, T.S. Lee, Synthesis of chemically bound conjugated polymer on TiO$_2$ for a visible-light-driven photocatalyst: Changeable surface wettability, Mater. Des. 203 (2021) 109630, https://doi.org/10.1016/j.matdes.2021.109630.

[29] D. Bhalothia, Z.X. Wang, L.Y. Ting, Y.T. Chuang, J.P. Chou, H.W. Lin, F.G. Tseng, H.H. Chou, T.Y. Chen, Electron coupling between the linear-conjugated polymer nanocluster and TiO$_2$ nanoparticle enables a quantum leap for visible light-driven hydrogen evolution, J. Phys. Chem. C. 126 (2022) 18596–18604, https://doi.org/10.1021/acs.jpcc.2c05862.

[30] P.A. Van Hal, M.P.T. Christiaans, M.M. Wienk, J.M. Kroon, R.A.J. Janssen, Photoinduced electron transfer from conjugated polymers to TiO$_2$, J. Phys. Chem. B. 103 (1999) 4352–4359, https://doi.org/10.1021/jp9901803.

[31] N. Thiwakornkitkul, T. Suteewong, Effect of morphology of titanium dioxide nanoparticles on photocatalytic activity, IOP Conf. Ser. Mater. Sci. Eng. 639 (2019), https://doi.org/10.1088/1757-899X/639/1/012021.

[32] M. Saket-Oskoui, M. Khatamian, Morphology and crystalline phase-controllable synthesis of titania nanoparticles via acrylamide gel method and their photocatalytic properties, Mater. Sci. Semicond. Process. 27 (2014) 103–113, https://doi.org/10.1016/j.mssp.2014.06.002.

[33] P. Allende-González, M.Á. Laguna-Bercero, L. Barrientos, M.L. Valenzuela, C. Díaz, Solid state tuning of TiO$_2$ morphology, crystal phase, and size through metal macromolecular complexes and its significance in the photocatalytic response, ACS Appl. Energy Mater. 1 (2018) 3159–3170, https://doi.org/10.1021/acsaem.8b00374.

[34] Y. Absalan, M. Gholizadeh, L. Butusov, I. Bratchikova, V. Kopylov, O. Kovalchukova, Titania nanotubes (TNTs) prepared through the complex compound of gallic acid with titanium; examining photocatalytic degradation of the obtained TNTs, Arab. J. Chem. 13 (2020) 7274–7288, https://doi.org/10.1016/j.arabjc.2020.02.023.

[35] F. Akbal, Photocatalytic degradation of organic dyes in the presence of titanium dioxide under UV and solar light : effect of operational, Environ. Prog. 24 (2005) 317–322, https://doi.org/10.1002/ep.10092.

[36] W.K. Jo, R.J. Tayade, New generation energy-efficient light source for photocatalysis: LEDs for environmental applications, Ind. Eng. Chem. Res. 53 (2014) 2073–2084, https://doi.org/10.1021/ie404176g.

[37] H. Chen, Y. Cheng, C.I. Moraru, Blue 405 nm LED light effectively inactivates bacterial pathogens on substrates and packaging materials used in food processing, Sci. Rep. 13 (2023) 15472, https://doi.org/10.1038/s41598-023-42347-z.

[38] M. Martín-sómer, C. Pablos, C. Adán, R. Van Grieken, J. Marugán, Science of the total environment a review on led technology in water photodisinfection, Sci. Total Environ. 885 (2023) 163963, https://doi.org/10.1016/j.scitotenv.2023.163963.

[39] M. Kang, G. Lee, I. Hwan, M. Yang, M. Beom, J. Choi, T. Geol, C. Yoon, B. Baek, M. Sung, D. Kim, E. Park, Uptake and toxicity of cerium dioxide nanoparticles with different aspect ratio, Toxicol. Lett. 373 (2023) 196–209, https://doi.org/10.1016/j.toxlet.2022.11.013.

[40] N.I. Politova-Brinkova, S.R. Tsibranska-Gyoreva, S.S. Tcholakova, N.D. Denkov, T. Danner, Preparation of TiO$_2$ nanoparticle aggregates and capsules by the 'two-emulsion method', Colloids Interf. 4 (2020) 57, https://doi.org/10.3390/colloids4040057.

[41] S.F. Shaikh, R.S. Mane, B.K. Min, Y.J. Hwang, O.S. Joo, D-sorbitol-induced phase control of TiO$_2$ nanoparticles and its application for dye-sensitized solar cells, Sci. Rep. 6 (2016) 1–10, https://doi.org/10.1038/srep20103.

[42] D.A.H. Hanaor, C.C. Sorrell, Review of the anatase to rutile phase transformation, J. Mater. Sci. 46 (2011) 855–874, https://doi.org/10.1007/s10853-010-5113-0.

[43] A.A. Gribb, J.F. Banfield, Particle size effects on transformation kinetics and phase stability in nanocrystalline TiO$_2$, Am. Mineral. 82 (1997) 717–728, https://doi.org/10.2138/am-1997-7-809.

[44] J. Saari, H. Ali-Löytty, K. Lahtonen, M. Hannula, L. Palmolahti, A. Tukiainen, M. Valden, Low-temperature route to direct amorphous to rutile crystallization of TiO$_2$ thin films grown by atomic layer deposition, J. Phys. Chem. C. 126 (2022) 15357–15366, https://doi.org/10.1021/acs.jpcc.2c04905.

[45] C. Byrne, R. Fagan, S. Hinder, D.E. McCormack, S.C. Pillai, New approach of modifying the anatase to rutile transition temperature in TiO$_2$ photocatalysts, RSC Adv. 6 (2016) 95232–95238, https://doi.org/10.1039/c6ra19759k.

[46] K. Sabyrov, N.D. Burrows, R.L. Penn, Size-dependent anatase to rutile phase transformation and particle growth, Chem. Mater. 25 (2013) 1408–1415, https://doi.org/10.1021/cm302129a.

[47] W. Li, C. Ni, H. Lin, C.P. Huang, S.I. Shah, Size dependence of thermal stability of TiO$_2$ nanoparticles, J. Appl. Phys. 96 (2004) 6663–6668, https://doi.org/10.1063/1.1807520.

[48] A. Navrotsky, O.J. Kleppa, Enthalpy of the Anatase-Rutile Transformation, J. Am. Ceram. Soc. 50 (1967) 626, https://doi.org/10.1111/j.1151-2916.1967.tb15013.x.

[49] H. Zhang, J.F. Banfield, Understanding polymorphic phase transformation behavior during growth of nanocrystalline aggregates: Insights from TiO$_2$, J. Phys. Chem. B. 104 (2000) 3481–3487, https://doi.org/10.1021/jp000499j.

[50] M. Germain, P. Fraundorf, S. Lin, E.A. Guliants, C.E. Bunker, S.W. Buckner, Synthesis and characterization of srilankite nanowires, J. Nanosci. Nanotechnol. 8 (2008) 1481–1488, https://doi.org/10.1166/jnn.2008.193.

[51] A. Willgallis, Hydrothermal Synthesis of (Zr$_{0.33}$Ti$_{0.67}$)O$_2$ - Srilankite in the System Zr02-Ti02-H20-MF; (M = Na, K), Cryst. Res. Technol. 24 (1989) 263–268, https://doi.org/10.1002/crat.2170240305.

[52] A.K. Bhattacharya, K.K. Mallick, A. Hartridge, J.L. Woodhead, Sol gel preparation, structure and thermal stability of crystalline zirconium titanate microspheres, J. Mater. Sci. 31 (1996) 267–271, https://doi.org/10.1007/BF00355155.

[53] A. Behbahani, S. Rowshanzamir, A. Esmaeilifar, Hydrothermal synthesis of zirconia nanoparticles from commercial zirconia, Procedia Eng. 42 (2012) 908–917, https://doi.org/10.1016/j.proeng.2012.07.483.

[54] S. Jayakumar, P.V. Ananthapadmanabhan, T.K. Thiyagarajan, K. Perumal, S.C. Mishra, G. Suresh, L.T. Su, A.I.Y. Tok, Nanosize stabilization of cubic and tetragonal phases in reactive plasma synthesized zirconia powders, Mater. Chem. Phys. 140 (2013) 176–182, https://doi.org/10.1016/j.matchemphys.2013.03.018.

[55] G. Katz, X-ray diffraction powder pattern of metastable cubic ZrO$_2$, J. Am. Ceram. Soc. 54 (1971) 531, https://doi.org/10.1111/j.1151-2916.1971.tb12197.x.

[56] P. Ying, M. Li, F. Yu, Y. Geng, L. Zhang, J. He, Y. Zheng, R. Chen, Band gap engineering in an efficient solar-driven interfacial evaporation system, ACS Appl. Mater. Interf. 12 (2020) 32880–32887, https://doi.org/10.1021/acsami.0c09965.

[57] Y. Nosaka, A.Y. Nosaka, Reconsideration of intrinsic band alignments within anatase and rutile TiO$_2$, J. Phys. Chem. Lett. 7 (2016) 7–10, https://doi.org/10.1021/acs.jpclett.5b02804.

[58] F. Gallino, C. Di Valentin, G. Pacchioni, Band gap engineering of bulk ZrO$_2$ by Ti doping, Phys. Chem. Chem. Phys. 13 (2011) 17667–17675, https://doi.org/10.1039/c1cp21987a.

[59] B. Gao, T.M. Lim, D.P. Subagio, T. Lim, Zr-doped TiO$_2$ for enhanced photocatalytic degradation of bisphenol A, Appl. Catal. A Gen. 375 (2010) 107–115, https://doi.org/10.1016/j.apcata.2009.12.025.

[60] W. Awin, S. Keshari, R. Kumar, Anomalous reduction in the band gap of zirconium titanate based composites, Mater. Lett. 251 (2019) 230–233, https://doi.org/10.1016/j.matlet.2019.05.063.

[61] D.J. Miller, M.C. Biesinger, N.S. McIntyre, Interactions of CO$_2$ and CO at fractional atmosphere pressures with iron and iron oxide surfaces: one possible mechanism for surface contamination? Surf. Interface Anal. 33 (2002) 299–305, https://doi.org/10.1002/sia.1188.

[62] A. Álvarez, M. Borges, J.J. Corral-Pérez, J.G. Olcina, L. Hu, D. Cornu, R. Huang, D. Stoian, A. Urakawa, CO$_2$ Activation over catalytic surfaces, ChemPhysChem. 18 (2017) 3135–3141, https://doi.org/10.1002/cphc.201700782.

[63] G. Zhang, Y. Zhou, Y. Yang, T. Yang, Y. Song, S. Zhang, H. Zheng, Elucidating the role of surface Ce4+ and oxygen vacancies of, Molecules. 28 (2023) 3785, https://doi.org/10.3390/molecules28093785.

[64] L.F. Bobadilla, J.L. Santos, S. Ivanova, J.A. Odriozola, A. Urakawa, Unravelling the role of oxygen vacancies in the mechanism of the reverse water-gas shift reaction by operando DRIFTS and ultraviolet-visible spectroscopy, ACS Catal. 8 (2018) 7455–7467, https://doi.org/10.1021/acscatal.8b02121.

[65] C. Zhang, L. Wang, U.J. Etim, Y. Song, O.M. Gazit, Z. Zhong, Oxygen vacancies in Cu/TiO$_2$ boost strong metal-support interaction and CO$_2$ hydrogenation to methanol, J. Catal. 413 (2022) 284–296, https://doi.org/10.1016/j.jcat.2022.06.026.

[66] U.J. Etim, C. Zhang, Z. Zhong, Impacts of the catalyst structures on CO$_2$ activation on catalyst surfaces, Nanomaterials. 11 (2021) 1–40, https://doi.org/10.3390/nano11123265.

[67] L.S. Gao, S.N. Zhang, X. Zou, J. Wang, J. Su, J.S. Chen, Oxygen vacancy engineering of titania-induced by Sr2+dopants for visible-light-driven hydrogen evolution, Inorg. Chem. 60 (2021) 32–36, https://doi.org/10.1021/acs.inorgchem.0c03325.

[68] N.A. Badli, R. Ali, W.A. Wan Abu Bakar, L. Yuliati, Role of heterojunction ZrTiO$_4$/ZrTi$_2$O$_6$/TiO$_2$ photocatalyst towards the degradation of paraquat dichloride and optimization study by Box-Behnken design, Arab. J. Chem. 10 (2017) 935–943, https://doi.org/10.1016/j.arabjc.2016.02.011.

[69] E.H. Mourid, E.M. El Mountassir, L. El Mersly, L. Benaziz, S. Rafqah, M. Lakraimi, Development of a new recyclable nanocomoposite LDH-TiO$_2$ for the degradation of antibiotic sulfamethoxazole under UVA radiation: An approach towards sunlight, J. Photochem. Photobiol. A Chem. 396 (2020) 112530, https://doi.org/10.1016/j.jphotochem.2020.112530.

[70] H. Deb, M. Neaz Morshed, X. Shili, S. Al Azad, Z. Cai, A. Ahmed, Design and development of -TiO$_2$-Fe0 nanoparticle-immobilized nanofibrous mat for photocatalytic degradation of hazardous water pollutants, J. Mater. Sci. Mater. Electron. 30 (2019) 4842–4854, https://doi.org/10.1007/s10854-019-00779-2.

[71] L.A.J. Rodríguez-Blanco, R. Ocampo-Pérez, C.F.A. Gómez-Durán, J.P. Mojica-Sánchez, R.S. Razo-Hernández, Removal of sulfamethoxazole, sulfadiazine, and sulfamethazine by UV radiation and HO• and SO4•− radicals using a response surface model and DFT calculations, Environ. Sci. Pollut. Res. 27 (2020) 41609–41622, https://doi.org/10.1007/s11356-020-10071-0.

[72] J. Tian, Q. Shao, J. Zhao, D. Pan, M. Dong, C. Jia, T. Ding, T. Wu, Z. Guo, Microwave solvothermal carboxymethyl chitosan templated synthesis of TiO_2/ZrO_2 composites toward enhanced photocatalytic degradation of Rhodamine B, Z. Guo), J. Colloid Interface Sci. 541 (2019) 18–29, https://doi.org/10.1016/j.jcis.2019.01.069.

[73] B.M. Pirzada, N.A. Mir, N. Qutub, O. Mehraj, S. Sabir, M. Muneer, Synthesis, characterization and optimization of photocatalytic activity of TiO_2/ZrO_2 nanocomposite heterostructures, Mater. Sci. Eng. B Solid-State Mater. Adv. Technol. 193 (2015) 137–145, https://doi.org/10.1016/j.mseb.2014.12.005.

[74] C.F. Carbuloni, J.E. Savoia, J.S.P. Santos, C.A.A. Pereira, R.G. Marques, V.A. S. Ribeiro, A.M. Ferrari, Degradation of metformin in water by TiO_2–ZrO_2 photocatalysis, J. Environ. Manage. 262 (2020) 110347, https://doi.org/10.1016/J.JENVMAN.2020.110347.

[75] J. Abdi, M. Yahyanezhad, S. Sakhaie, M. Vossoughi, I. Alemzadeh, Synthesis of porous TiO_2/ZrO_2 photocatalyst derived from zirconium metal organic framework for degradation of organic pollutants under visible light irradiation, J. Environ. Chem. Eng. 7 (2019) 103096, https://doi.org/10.1016/J.JECE.2019.103096.

[76] A. Mbiri, G. Wittstock, D.H. Taffa, E. Gatebe, J. Baya, M. Wark, Photocatalytic degradation of the herbicide chloridazon on mesoporous titania/zirconia nanopowders, Environ. Sci. Pollut. Res. 25 (2018) 34873–34883, https://doi.org/10.1007/S11356-017-1023-X/FIGURES/7.

[77] J. Zheng, L. Sun, C. Jiao, Q. Shao, J. Lin, D. Pan, N. Naik, Z. Guo, Hydrothermally synthesized Ti/Zr bimetallic MOFs derived N self-doped TiO_2/ZrO_2 composite catalysts with enhanced photocatalytic degradation of methylene blue, Colloids Surf. A Physicochem. Eng. Asp. 623 (2021) 126629, https://doi.org/10.1016/J.COLSURFA.2021.126629.

[78] J. Lang, L. Matějová, Z. Matěj, L. Čapek, A. Martaus, M. Kormunda, The effect of Zr loading in Zr/TiO_2 prepared by pressurized hot water on its surface, morphological and photocatalytic properties, J. Sol-Gel Sci. Technol. (2019), https://doi.org/10.1007/s10971-019-04956-x.